Nanotopography Influences Adhesion, Spreading, and Self-Renewal of Human Embryonic Stem Cells

Weiqiang Chen,[†,‡] Luis G. Villa-Diaz,[§] Yubing Sun,[†,‡] Shinuo Weng,[†,‡] Jin Koo Kim,[§] Raymond H. W. Lam,[†,‡,⊥] Lin Han,[∥] Rong Fan,[∥] Paul H. Krebsbach,[§,#] and Jianping Fu[†,‡,#,*]

[†]Integrated Biosystems and Biomechanics Laboratory, University of Michigan, Ann Arbor, Michigan 48109, United States, [‡]Department of Mechanical Engineering, University of Michigan, Ann Arbor, Michigan 48109, United States, [§]Department of Biologic and Materials Sciences, University of Michigan, Ann Arbor, Michigan 48109, United States, [⊥]Department of Mechanical and Biomedical Engineering, City University of Hong Kong, Hong Kong, People's Republic of China, [∥]Department of Biomedical Engineering, Yale University, New Haven, Connecticut 06511, United States, and [#]Department of Biomedical Engineering, University of Michigan, Ann Arbor, Michigan 48109, United States

ABSTRACT

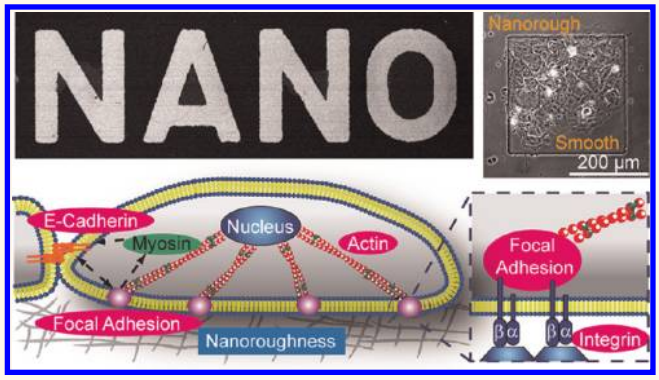

Human embryonic stem cells (hESCs) have great potentials for future cell-based therapeutics. However, their mechanosensitivity to biophysical signals from the cellular microenvironment is not well characterized. Here we introduced an effective microfabrication strategy for accurate control and patterning of nanoroughness on glass surfaces. Our results demonstrated that nanotopography could provide a potent regulatory signal over different hESC behaviors, including cell morphology, adhesion, proliferation, clonal expansion, and self-renewal. Our results indicated that topological sensing of hESCs might include feedback regulation involving mechanosensory integrin-mediated cell–matrix adhesion, myosin II, and E-cadherin. Our results also demonstrated that cellular responses to nanotopography were cell-type specific, and as such, we could generate a spatially segregated coculture system for hESCs and NIH/3T3 fibroblasts using patterned nanorough glass surfaces.

KEYWORDS: human embryonic stem cell · nanotopography · microfabrication · mechanosensitivity · self-renewal

Cells that adhere to the extracellular matrix (ECM) can sense and respond to a wide variety of chemical and physical features of the adhesive surface, including the molecular nature of adhesive ligands and their local densities, as well as surface topography and rigidity.[1−8] Topological sensing, the capacity to differentially respond to substrates with varying degrees of topology, is a general phenomenon affecting multiple cellular properties including morphology, migratory capacity, gene expression profile, and, eventually, cell differentiation and fate.[9,10]

Recent reports have shown that the nanoscale surface topography plays a critical role in regulating survival, proliferation, and differentiation of various types of adult multipotent stem cells.[11−16] For example, human mesenchymal stem cells (hMSCs) cultured on nanoscale gratings on polydimethylsiloxane surfaces tend to align and elongate their actin cytoskeleton (CSK) and nuclei along the nanogratings.[13] Likewise, gene profiling and immunostaining of these hMSCs demonstrate a significant upregulation of neuronal markers when cultured on the nanogratings, as compared to unpatterned flat controls.[13] Recent published reports have also demonstrated that the nanoscale disorder in a nanopit array can stimulate osteogenesis of hMSCs in the absence of osteogenic supplements,[12] while another study from the same group verifies that the perfectly ordered arrays of nanopits support long-term maintenance of hMSC phenotype and multipotency.[15]

Only in the past few years has experimental evidence begun to emerge showing that pluripotent stem cells such as embryonic stem cells (ESCs) are sensitive to the cell–ECM physical interactions,[17−23] including their intrinsic sensitivity to the nanoscale surface topography.[22,23] These early findings have promoted significant interest from the developing fields of functional tissue engineering and regenerative medicine, as ESCs are able to replicate themselves (self-renewal) while retaining their ability to give

* Address correspondence to jpfu@umich.edu.

Received for review February 2, 2012 and accepted April 9, 2012.

Published online April 09, 2012
10.1021/nn3004923

rise to any type of specialized cell in the adult body (pluripotency),[24−26] and as such, human ESCs (hESCs) are a promising cell source for disease modeling,[27,28] drug screenings,[29−31] and future cell-based therapeutics to treat degenerative human diseases such as diabetes mellitus and trauma such as spinal cord injury.[32−35]

To date, the existing work on regulation of ESC behaviors using nanotopography has focused on their neurogenic differentiation with regularly arranged nanoscale surface structures. For example, it has been shown that the electrospun fibrous scaffolds can not only enhance differentiation of mouse ESCs (mESCs) into specific neural lineages but also promote and guide the neurite outgrowth.[22] More recently, nanoscale ridge/groove pattern arrays generated on polyurethane acrylate surfaces are shown to induce morphological changes and differentiation of hESCs into a neuronal lineage without treatment with differentiation-inducing biochemical agents.[23]

However, all the aforementioned work on nanotopography for stem cells has largely relied on complex and expensive nanofabrication techniques, such as electron beam and nanoimprint lithography, to generate nanoscale surface structures to regulate cell−ECM interactions. Further, it is still largely unknown to what extent such synthetic regular nanoscale structures can mimic the intrinsic random nanoscale topology associated with the *in vivo* cellular microenvironment. Herein, we developed an effective microfabrication method for precise control and spatial patterning of local nanoroughness on glass substrates using standard photolithography and reactive ion etching (RIE) techniques. Using our RIE-generated nanorough glass surfaces, we demonstrated that the nanoscale surface roughness is a potent physical signal in the cellular microenvironment to regulate a diverse array of hESC behaviors, including their morphology, cell adhesion, self-renewal, and pluripotency. Our experimental results further suggested the involvement of integrin-mediated focal adhesion (FA), myosin II activity, and E-cadherin-mediated cell−cell contacts in regulating topological sensing of hESCs.

RESULTS AND DISCUSSION

Fabrication Method. In this work, the surface nanoroughness on the silica-based glass wafers (Borofloat 33 glass) was generated with RIE, a well-established process used in semiconductor microfabrication (Figure 1). The etching of the silica-based glass wafer was consistent with a process of the ion-enhanced chemical reaction and physical sputtering as reported by others.[36,37] Specifically, during the RIE process, bombardment by the reactive ion species generated using the SF_6 and C_4F_8 gases disrupted the unreactive glass substrate and caused damage such as dangling

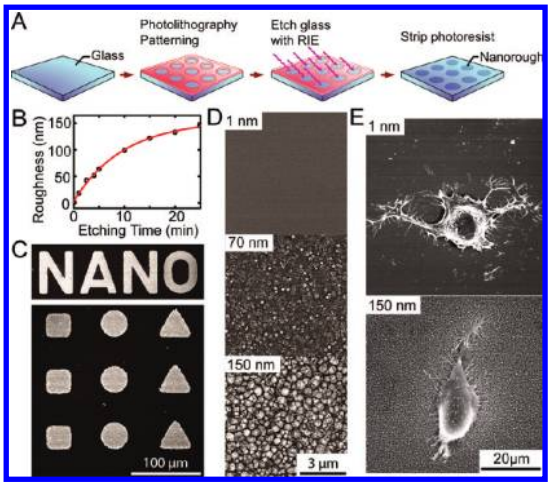

Figure 1. (A) Schematic of the fabrication process for patterned nanorough glass substrates using photolithography followed by RIE. (B) Nanoscale surface roughness generated on glass substrates using RIE as a function of the RIE process time, with a red fitting curve plotted for guidance. (C) SEM images of glass surfaces patterned with nanorough letters (NANO; top) and different shaped islands (bottom) using photolithography followed by RIE. (D) High-resolution SEM images of glass surfaces without (top) or with (middle and bottom) treatments of RIE-based surface-roughening processes, with their rms nanoroughness indicated. (E) SEM images of single hESCs plated on smooth (R_q = 1 nm) and nanorough (R_q = 150 nm) glass surfaces. The cells were fixed after culture of 24 h on the glass surfaces.

bonds and dislocations, resulting in the glass surface being reactive toward the etchant species. Interestingly, since small concentrations of impurities such as Al, K, and Na (about 6% w/w in total) existed in the silica glass, these impurities resulted in accumulations of less volatile species (such as AlF_3, KF, NaF) on the glass surface during the RIE process.[36,37] Thus, when the reactive plasma species approached the glass surface, these less volatile compounds inevitably underwent numerous collisions with the plasma species. Some of these compounds were then backscattered onto the glass surface and formed randomly distributed small clusters that could shield the glass surface from bombardment and reaction with reactive ions. These compound clusters effectively generated the so-called "micromasking" effect that could randomly shadow the glass surface and thus result in nanoscale roughening of the glass surface during the RIE process.[36] Therefore, under the same RIE process conditions, the surface nanoroughness of the glass wafer could be precisely controlled on the nanoscale by solely adjusting the RIE process duration.

The initial surface roughness of the unprocessed silica-based glass wafers, characterized by atomic force microscope (AFM) using the root-mean-square (rms) roughness R_q (see Methods for details of fabrication and surface characterization of nanorough glass samples), was about 1 nm. The glass wafers were processed with RIE (LAM 9400, Lam Research, Fremont, CA, USA) for different periods of time to generate

nanorough surfaces with R_q ranging from 1 to 150 nm (Figure 1A), using SF_6, C_4F_8, He, and Ar gas mixtures. To spatially pattern nanoroughness on the glass wafers, the glass wafers were first spin-coated with photoresist, and the photoresist layer was then patterned with photolithography to physically expose different glass regions of various sizes and shapes for subsequent RIE etching. After the RIE process, photoresist was stripped using solvents, and the glass wafers were cleaned using distilled water and a Piranha solution (4:1 H_2SO_4/H_2O_2) to remove organic residues from the glass substrates.[38] Thus, by precisely controlling photolithography and RIE, we could specify the location, shape, area, and nanoroughness level of different nanorough regions on glass substrates (Figure 1A–C).

Functional Responses of hESC. Using the nanorough glass substrates described above, we first examined functional responses of hESCs to different levels of nanoroughness, including their morphology, adhesion, proliferation, clonal expansion, and differentiation. Here, all glass substrates were precoated with vitronectin (5 μg/mL) by adsorption to support long-term self-renewal of hESCs as reported by others.[39] Using AFM, we confirmed that the rms roughness R_q of the smooth and nanorough glass surfaces did not significantly change before and after vitronectin coating (Supplemental Figure S1A,B). To further confirm that the density of the adsorbed vitronectin on the glass surfaces was independent of the nanoroughness R_q of the glass surface, control assays were performed. Using fluorophore-labeled proteins, no apparent difference in fluorescence intensity was observed between glass surfaces of different nanoroughness R_q, indicating constant protein densities on the glass surfaces (Supplemental Figure S1C,D).

Scanning electron microscopy (SEM) images of single hESCs demonstrated that hESCs exhibited distinct morphological features on smooth and nanorough glass surfaces 24 h after cell seeding. A highly branched, filopodia-rich morphology of single hESCs was observed on the smooth glass surface (R_q = 1 nm; Figure 1E, top) as compared to the more compact cells with few, short cytoplasmic extensions on the nanorough surface (R_q = 150 nm; Figure 1E, bottom). Additionally, hESCs demonstrated significant adhesion selectivity between different levels of nanoroughness on the glass surfaces. For example, after 48 h of culture on a glass surface patterned with square-shaped, smooth islands surrounded by nanorough surfaces, hESCs selectively adhered to, and aggregated on, the smooth islands where R_q = 1 nm, but not on the nanorough areas where R_q = 70 nm (Figure 2A). During this selective adhesion and aggregation process, hESCs retained their stemness, as evidenced by their positive expression of Oct3/4 (Oct3/4+), a transcription factor and a hallmark of undifferentiated hESCs (Figure 2A). Interestingly, spontaneously differentiated hESCs, which would lose their expression of Oct3/4 (Oct3/4−), did not show any adhesion preference to either the smooth or nanorough surfaces, and Oct3/4− hESCs would randomly distribute on the patterned glass substrate (Figure 2B).

We quantified the cell adhesion rate, defined as the ratio of number of cells adhered to the glass surface to the total number of cells initially seeded, of single Oct3/4+ hESCs plated on glass substrates with different values of R_q. Our results showed that 24 h after cell seeding, Oct3/4+ hESCs at the single-cell level had a strong tendency to adhere to smooth glass surfaces with smaller R_q (Figure 2C). In contrast, Oct3/4+ hESCs adhered less to surfaces with an increasing R_q. Both phenomena were consistent regardless of treatment with or without Y27632, a Rho-associated coil kinase (ROCK) inhibitor used to enhance survival of single fully dissociated hESCs (Figure 2C).

The effect of topological sensing of hESCs on their self-renewal and stemness maintenance was also investigated. In the experiments, Oct3/4+ hESCs were seeded at a low density (5×10^3 cells/cm^2) on both smooth (R_q = 1 nm) and nanorough (R_q = 150 nm) glass surfaces and cultured for 7 days. Subsequently, cells were fixed and stained with 4′,6-diamidino-2-phenylindole (DAPI) to identify nuclei and fluorescent-labeled antibodies for Oct3/4 (Figure 2F). Quantification of Oct3/4+ hESCs as a function of R_q showed a higher percentage of Oct3/4+ cells (93.6%) on the smooth glass surface (R_q = 1 nm) as compared to cells seeded on nanorough surfaces (41% and 36.6% for R_q = 70 and 150 nm, respectively; Figure 2D). Thus, our results indicated that the smooth glass surface was conducive to self-renewal and maintenance of hESC stemness in long-term culture, while the nanorough glass surfaces resulted in a large portion of hESCs undergoing spontaneous differentiation, thus losing their pluripotency (Figure 2D,F).

To investigate the extent to which nanoscale topological cues could affect proliferation of hESCs, small clusters of undifferentiated hESCs were seeded on glass substrates with different values of R_q (1, 70, and 150 nm) and observed for 7 days. Phase-contrast microscopic images of hESC colonies were taken 1, 2, 3, and 5 days after cell seeding for these different glass substrates. Owing to their self-renewal, colonies of hESCs on these glass substrates would continuously grow during this 7-day observation period. Colony sizes were analyzed using these colony images with the image analysis software ImageJ to calculate the cell population doubling time. hESCs proliferated more rapidly with a shortened cell population doubling time of 41 h on the smooth glass surface (R_q = 1 nm) as compared to cells on the RIE-generated nanorough surfaces, on which the cell population doubling time was 71 h for R_q = 70 nm and 77 h for R_q = 150 nm (Figure 2E,G). Together, these results confirmed that

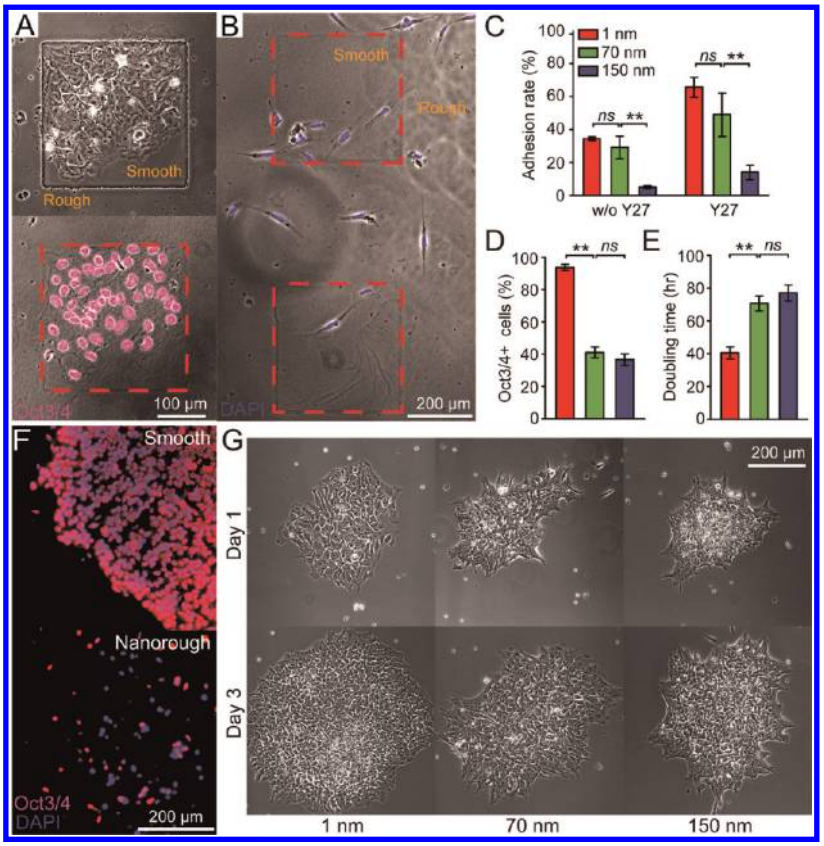

Figure 2. (A) Representative phase-contrast (top) and merged (bottom) microscopic images showing Oct3/4+ hESCs selectively attached and aggregated on the smooth region (R_q = 1 nm) of a patterned nanorough glass substrate. (B) Representative merged microscopic image showing Oct3/4− hESCs randomly distributed on a patterned nanorough glass surface without showing a preference for either smooth or nanorough areas. For A and B, the nanorough regions of the glass substrate had a rms R_q of 70 nm. Cells were cultured 48 h after initial cell seeding and costained with DAPI for nuclei (blue) and Oct3/4 (red). (C) Adhesion rate of single hESCs after 24 h of culture on glass substrates with different levels of nanoroughness. Cells were treated with or without Y27632 (Y27) as indicated. Error bars represent ±standard error of the mean (SE, n = 3). (D) Percentage of Oct3/4+ hESCs on the glass substrates with different levels of nanoroughness as indicated, after culture for 7 days. Error bars represent ±SE (n = 3). (E) Doubling time of hESCs on the glass substrates with different levels of nanoroughness as indicated. Error bars represent ±SE (n = 20). For C−E, *ns* (> 0.05) and ** (p < 0.01) (Student's t-test). (F) Representative immunofluorescence images of hESCs cultured for 7 days on both the smooth (R_q = 1 nm; top) and nanorough (R_q = 150 nm; bottom) glass substrates. The cells were costained for Oct3/4 (red) and nuclei (DAPI; blue). (G) Representative phase-contrast microscopic images of hESC colonies on smooth (R_q = 1 nm; left) and nanorough (R_q = 70 and 150 nm; middle and right) glass substrates after culture of 1 day (top) and 3 days (bottom).

the nanotopological cue on the RIE-generated glass surface to which hESCs adhered could provide a potent regulatory signal that affects a diverse array of hESC behaviors including cell morphology, adhesion, proliferation, and self-renewal.

Topological Sensing by FAs, CSK Structure, and Cell−Cell Contacts. The molecular mechanism for topological sensing by adherent cells remains largely undetermined, yet existing evidence from different cell types has suggested the involvement of integrin-mediated focal adhesion signaling.[2] Integrins mediate cell adhesion to the ECM and contribute to cell−matrix signaling by activating intracellular tyrosine kinase and phosphatase signaling to elicit downstream biochemical signals important for regulation of gene expression and stem cell fate. Importantly, integrin-mediated FA signaling is closely related to its molecular arrangement and dynamic organization, which can be affected directly by local nanotopological cues.[2]

To investigate the likely involvement of integrin-mediated FA formation in regulating topological sensing of hESCs, we examined FA formation of single hESCs plated on nanorough glass surfaces. After 48 h of culture, single hESCs exhibited distinct FA formations and organizations on the smooth and nanorough glass surfaces, as characterized by immunofluorescence staining of vinculin, a FA protein. On smooth glass surfaces, where R_q = 1 nm, vinculin-containing FAs formed primarily on the periphery of undifferentiated hESCs (Oct3/4+) but distributed randomly throughout the whole cell spread area of differentiated cells (Oct3/4−) (Figure 3A). However, on the nanorough surface where R_q = 100 nm, both Oct3/4+ and Oct3/4− hESCs exhibited randomly distributed, punctate FAs of small areas throughout the entire cell spread area (Figure 3A). Morphometric analysis of cell populations suggested that on the smooth glass surface Oct3/4− hESCs had a smaller mean cell spread area than Oct3/4+ hESCs, and

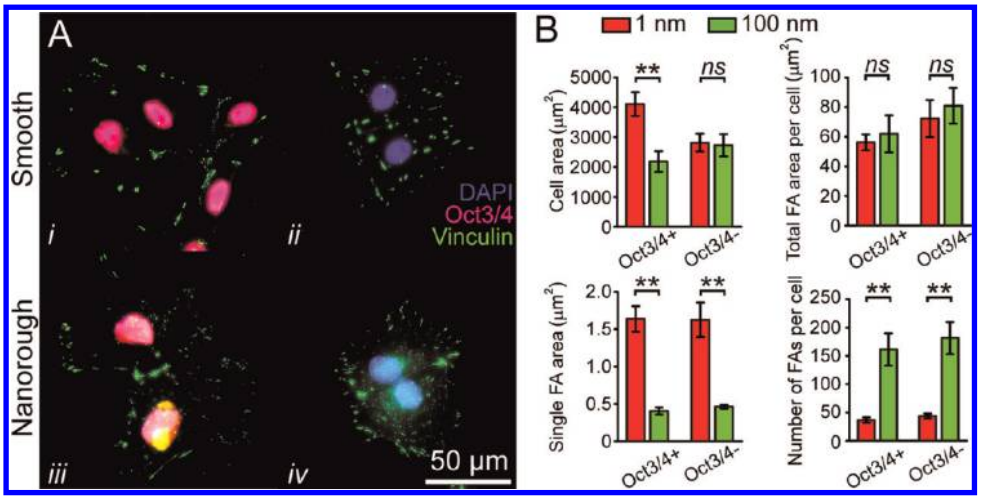

Figure 3. (A) Representative immunofluorescence images of Oct3/4+ (*i* and *iii*) and Oct3/4− (*ii* and *iv*) hESCs on smooth (R_q = 1 nm) and nanorough (R_q = 100 nm) glass substrates after 48 h of culture. Cells were costained for nuclei (DAPI; blue), Oct3/4 (red), and vinculin (green). (B) Bar graphs showing quantitative results of cell spread area (top left), total FA area per cell (top right), average single FA area (bottom left), and number of FAs per cell (bottom right) for Oct3/4+ and Oct3/4− hESCs cultured on glass substrates with different levels of nanoroughness as indicated. Error bars represent ± SE (n = 50). *ns* (p > 0.05), ** (p < 0.01); Student's *t*-test.

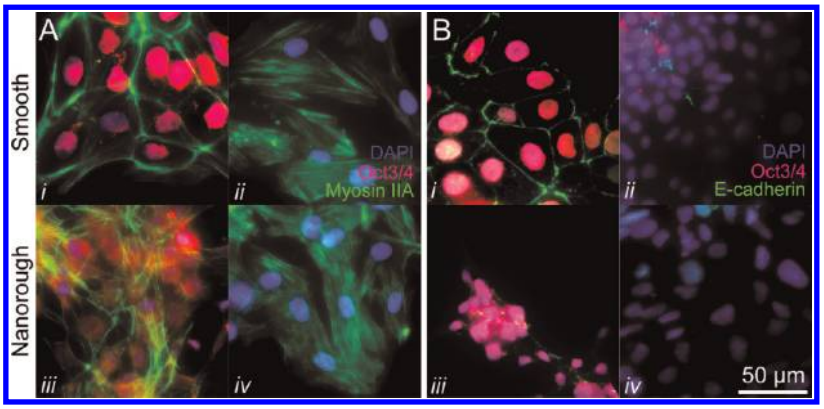

Figure 4. Representative immunofluorescence images of Oct3/4+ (*i* and *iii*) and Oct3/4− (*ii* and *iv*) hESCs on smooth (R_q = 1 nm) or nanorough (R_q = 100 nm) glass surfaces after culture of 48 h. The cells were costained for nuclei (DAPI; blue), Oct3/4 (red), and myosin IIA (A; green) or E-cadherin (B; green).

the nanorough surface resulted in both Oct3/4+ and Oct3/4− hESCs having a small mean cell spread area comparable to Oct3/4− hESCs on the smooth glass surface. Furthermore, our results indicated that both Oct3/4+ and Oct3/4− hESCs on the nanorough surface formed FAs of smaller areas but with a greater density as compared with the cells on the smooth surface (Figure 3B). Collectively, our results indicated that the nanotopography significantly affected the molecular arrangement, formation, and distribution of FAs in hESCs (Figure 3).

Previous studies have suggested that nonmuscle myosin IIA (NMMIIA)-dependent CSK contractility is a key mediator of the mechano-sensing and -transduction processes in different types of stem cells.[18,40−42] For hESCs, recent studies show that the NMMIIA-mediated CSK contractility plays a critical role in regulating hESC survival and cloning efficiency by controlling E-cadherin-mediated intercellular adhesion of hESCs.[42−45] Thus, we hypothesized that a feedback regulation and mechanical−biochemical integration involving FA, NMMIIA, and E-cadherin might be engaged in topological sensing of hESCs by their cross-regulation of intercellular adhesion and cell−ECM interactions (Supplemental Figure S2). To examine this possibility, we examined NMMIIA (Figure 4A) and E-cadherin (Figure 4B) expressions in hESCs plated on both the smooth (R_q = 1 nm) and nanorough (R_q = 100 nm) glass substrates after 48 h of culture, by costaining the cells with Oct3/4 and DAPI. Subcellular organizations of NMMIIA and E-cadherin were distinct between Oct3/4+ and Oct3/4− hESCs on the smooth surface, where Oct3/4+ hESCs demonstrated strong expressions of NMMIIA and E-cadherin concentrating and colocalizing on the cell−cell contacts, while Oct3/4− cells displayed a random distribution of NMMIIA throughout the whole cell spread area and a low expression level for E-cadherin. Interestingly, regardless

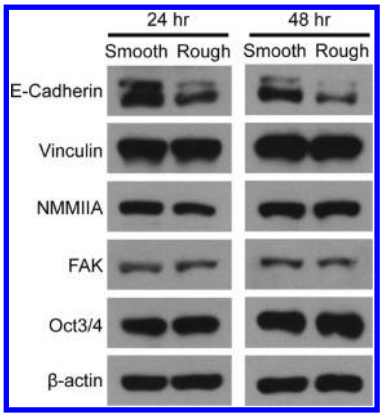

Figure 5. Western blot analysis of full-length E-cadherin, vinculin, NMMIIA, focal adhesion kinase (FAK), Oct3/4, and β-actin in Oct3/4+ hESCs plated on smooth (R_q = 1 nm) and nanorough (R_q = 100 nm) glass substrates after 24 h (left) and 48 h (right) of culture.

of the Oct3/4 expression levels, hESCs adhered to the nanorough surface demonstrated a random distribution of NMMIIA throughout the entire cells and a weak expression of E-cadherin, similar to Oct3/4− hESCs adhered on the smooth surface, suggesting that topological sensing and functional regulation by hESCs might involve the functional interplay between the mechanosensory components of FA, NMMIIA, and E-cadherin.

We further performed Western blot analysis of full-length E-cadherin, vinculin, NMMIIA, focal adhesion kinase (FAK; a kinase involved in regulating FA signaling), Oct3/4, and β-actin (as a housekeeping control protein) in Oct3/4+ hESCs plated on smooth (R_q = 1 nm) and nanorough (R_q = 100 nm) glass substrates after 24 and 48 h of culture. Our result suggested that for both time points the total amount of vinculin, NMMIIA, and FAK did not change between cells plated on smooth and nanorough surfaces (Figure 5). However, expression of E-cadherin was clearly down-regulated for hESCs plated on the nanorough surfaces as compared to cells on the smooth substrates, consistent with the immunostaining results shown in Figure 4. Combining the results in Figure 4 and Figure 5, it appeared that nanotopography might regulate hESC behaviors through its direct effect on the local molecular arrangement and formation of FAs that might in turn regulate the spatial organization of NMMIIA-mediated CSK contractility and the E-cadherin-mediated intercellular adhesion of hESCs, even though the total expression levels of FA proteins such as vinculin and NMMIIA might not be significantly affected by nanotopography. It was highly likely that E-cadherin-mediated cell−cell contacts of hESCs might serve as the downstream mediator to convert the nanotopographic signal through FAs and CSK contractility to regulate downstream gene expression and fate decisions of hESCs (Supplemental Figure S3).

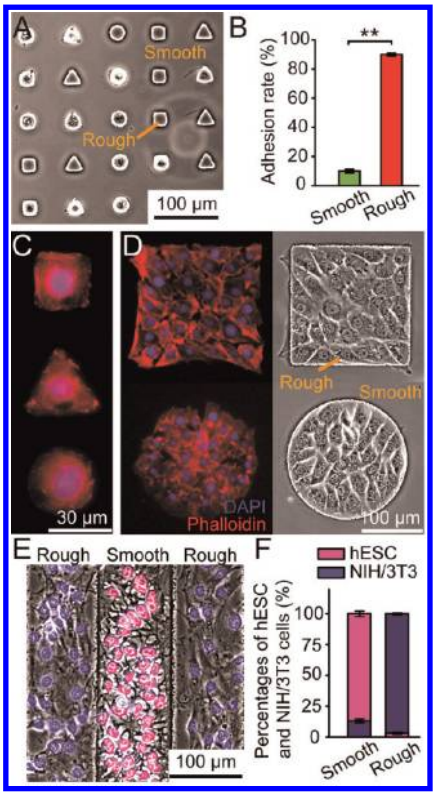

Figure 6. (A) Phase-contrast microscopic image of single NIH/3T3 fibroblasts adhered on patterned nanorough islands (R_q = 70 nm) on a glass substrate 4 h after initial cell seeding. (B) Bar graph showing the cell adhesion rate of single NIH/3T3 fibroblasts on the smooth surface (R_q = 1 nm) and the patterned nanorough islands (R_q = 70 nm) of a glass substrate. Error bars represent ± SE (n = 30). ** (p < 0.01); Student's t-test. (C) Immunofluorescence image showing single NIH/3T3 fibroblasts attaching and conforming to nanorough islands (R_q = 70 nm) of different geometries on the glass surface. The cells were fixed and stained 4 h after initial cell seeding. (D) Immunofluorescence (left) and phase-contrast (right) microscopic images of clusters of NIH/3T3 fibroblasts selectively attaching and conforming to nanorough islands (R_q = 70 nm) of different geometries on the glass surface. The images were taken 24 h after initial cell seeding. For C and D, cells were costained with DAPI (blue) and phalloidin (red) for visualization of nuclei and actin microfilaments, respectively. (E) Merged microscopic image showing cocultured Oct3/4+ hESCs and NIH/3T3 fibroblasts spatially self-segregating on a patterned nanorough glass surface after 48 h of culture. Cells were fixed and stained for nuclei (DAPI, blue) and Oct3/4 (red). The smooth and nanorough regions on the glass surface had rms R_q of 1 and 70 nm, respectively. (F) Bar graph showing percentages of hESCs and NIH/3T3 fibroblasts located on the smooth (R_q = 1 nm) and nanorough (R_q = 70 nm) regions of the patterned nanorough glass substrate after culture of 48 h. Error bars represent ± SE (n = 3).

Application to Cell Separation. To further explore the general phenomenon of topological sensing, experiments using the RIE-generated nanotopological glass surfaces were performed with NIH/3T3 fibroblasts. Phase-contrast and immunofluorescence images of single NIH/3T3 fibroblasts taken 4 h after cell seeding on a glass surface patterned with different shaped nanorough islands (R_q = 70 nm, with the surrounding areas smooth) showed that NIH/3T3 fibroblasts attached

preferentially to the patterned nanorough islands and spread to conform to the different geometries of the nanorough islands (Figure 6A–C). The adhesion selectivity of NIH/3T3 fibroblasts to the patterned nanorough islands was about 91% (Figure 6B), suggesting the patterned nanoroughness could serve as an effective means to control the adhesion location and cell shape or spread area of NIH/3T3 cells. In addition, when a high density of single NIH/3T3 fibroblasts were seeded on a glass surface patterned with large nanorough islands, the cells attached and aggregated to the patterned nanorough islands to form cell colonies that conformed to the different geometries of the nanorough islands (Figure 6D). Thus, the adhesion response of NIH/3T3 fibroblasts to nanotopography was completely contrary to that of hESCs (Figure 2A), indicating cell-type specificities in cellular responses to nanotopography.

The cell-type-specific preference to adhere to either smooth or nanorough surfaces provided an opportunity to spatially separate different cell types for cell coculture applications. To explore this prospect, a mixture of hESCs and NIH/3T3 fibroblasts was cultured on a patterned nanorough glass substrate containing an array of nanorough strips separated by smooth regions. The cell adhesion and separation on the patterned surface after coculturing the cells for 48 h was examined, showing that hESCs and NIH/3T3 fibroblasts selectively attached and autonomously segregated to the smooth and nanorough regions, respectively (Figure 6E). Quantitative analysis suggested a superior cell segregation efficiency for hESCs and NIH/3T3 cells using the patterned nanorough surfaces, as 87% of the cells adhered on the smooth regions of the glass surface were hESCs, while on the nanorough regions 97% of cells were NIH/3T3 fibroblasts (Figure 6F).

CONCLUSION

In this work, we report an effective microfabrication strategy for precise control and patterning of the local nanoroughness on glass surfaces using photolithography and RIE. It was demonstrated that hESCs were intrinsically sensitive to the nanoscale topological cues on the substrate. Also it was demonstrated that smooth glass surfaces supported cell adhesion, rapid cell proliferation, and long-term self-renewal of hESCs, while the nanorough glass surfaces tended to induce hESCs into spontaneous differentiation. Cell shape is a potent regulator of stem cell fate both *in vivo* and *in vitro*, and conventional studies have used microcontact printing and other methods to control cell shape and geometry.[40,46] In this work, we further generated nanorough patterns on glass surfaces and showed that such patterned nanoroughness could serve as an effective means for confining geometries or shapes of single hESCs or small hESC colonies. Our results further suggested that the cellular responses of hESCs to nanotopography might be functionally linked to their disrupted FA formation, NMMIIA activity, and E-cadherin-regulated intercellular adhesion. A feedback regulation and mechanical–biochemical integration mechanism involving these intracellular mechanosensory components might play an important role regulating hESC behavior during long-term self-renewal. In addition, it was demonstrated that cellular responses to nanotopography were cell-type specific, as NIH/3T3 fibroblasts appeared to adhere preferentially on nanorough surfaces as compared to smooth ones. By taking advantage of such cell-type-specific adhesion preference, a spatially segregated coculture system for hESCs and NIH/3T3 using patterned nanorough glass surfaces was demonstrated. Together, these results provide important insights into the mechanosensitivity of hESCs to nanotopological cues in the cellular microenvironment and further highlight the important role of well-designed and controlled synthetic stem cell microenvironment to direct hESC behaviors that are desirable for functional tissue engineering and regenerative medicine.

METHODS

Fabrication and Surface Characterization of Nanorough Glass Samples. Glass wafers (Borofloat 33, Plan Optik, Elsoff, Germany) were first spin-coated with photoresist. The photoresist layer was patterned using photolithography to physically expose different regions of the underlying glass wafer. The glass wafer was then processed with RIE (LAM 9400, Lam Research, Fremont, CA, USA) for different periods of time to generate the nanoscale surface roughness (ranging from 1 to 150 nm) on the open regions of the glass wafer, where the photoresist had previously been developed and dissolved. The corresponding RIE process conditions were selected: SF_6 (8 sccm), C_4F_8 (50 sccm), He (50 sccm), Ar (50 sccm), chamber pressure (1.33 Pa), bias voltage (100 V), and radio frequency power (500 W). The resulting glass etch rate by RIE was about 50 nm/min. After the RIE process, photoresist was stripped using solvents, and the glass wafer was cleaned using distilled water. For unpatterned nanorough glass samples, bare glass wafers were directly processed with RIE under the same RIE conditions as described above. All the processed glass wafers were cut into small pieces (1.5 cm × 1.5 cm) before assays with cells by using the ADT7100 dicing saw (Advanced Dicing Technologies Ltd., Yokneam, Israel).

Nanoroughness of the glass surfaces was measured at room temperature with the Veeco NanoMan Atomic Force Microscope (AFM, Digital Instruments Inc., Santa Barbara, CA, USA) using a noncontact, tapping mode and standard Si tapping mode AFP tips. The AFM scan image size for the glass surfaces was set as 10 μm × 10 μm with a scan rate of 1 Hz. The resulting map of the local surface height was represented using the AFM topographs. The nanoroughness of each glass sample was characterized by the root-mean-square roughness R_q of the local surface height over the scanned areas collected using the AFM topographs. The unprocessed bare glass wafer had an initial surface roughness R_q of 1 nm.

Cell Culture and Reagents. The glass substrates were functionalized with human vitronectin (R&D System, Minneapolis, MN, USA) by immersing the substrates in a vitronectin solution

(20 μg mL^{-1}) in distilled water overnight. The glass substrates were rinsed twice with PBS before they were used for cell seeding.

hESCs (H9; WiCell, Madison, WI, USA) were cultured on a feeder-free synthetic polymer coating (PMEDSAH)[47,48] with the Human-Cell-Conditioned Medium (hCCM, GlobalStem, Rockville, MD, USA) supplemented with human recombinant basic fibroblast growth factor (bFGF; GlobalStem) at 37 °C in 5% CO_2. hESC colonies were observed every 24 h using a Leica stereomicroscope (Leica Microsystems Inc., Buffalo Grove, IL, USA). Differentiated cells were removed mechanically using a sterile pulled-glass pipet. The culture medium was replaced every 24 h. Cultures were passaged every 4−7 days.

For the hESC colony-forming assay, large undifferentiated hESC colonies were selected and cut using the StemPro EZPassage disposable stem cell passaging tool (Invitrogen, Carlsbad, CA, USA) to achieve a homogeneous initial cell cluster size. Clusters (20−50) of hESCs were transferred onto the vitronectin-coated glass surfaces and cultured using hCCM.

For the single-cell assay undifferentiated hESC colonies were mechanically cut into small aggregates using a sterile pulled-glass pipet and collected in a 1.5 mL centrifuge tube. After centrifugation at 1000 rpm for 5 min and a brief washing with PBS, the cell aggregates were treated with 0.5 mL of 0.25% Trypsin-EDTA in PBS for 1 min. Then 1 mL of hCCM was added to stop trypsinization and was followed by an immediate centrifugation. The cell pellet was then fully dispersed in the hCCM containing the ROCK inhibitor Y27632 (10 μM; Tocris Bioscience, Ellisville, MO, USA) and passed through a cell strainer with the 40 μm nylon mesh (BD Biosciences, Bedford, MA, USA) to remove large cell aggregates and thus obtain single hESCs. Y-27632 was used to enhance the survival rate of fully disassociated single hESCs during cell seeding. Single hESCs were then seeded at a low density (5000 cells/cm^2) onto the glass substrates and were then allowed to spread out overnight before other assays.

For immunostaining to visualize NMMIIA and E-Cadherin, hESCs were seeded on the glass substrates and cultivated in hCCM for the first 24 h. The cell media were then replaced with the bFGF-free hCCM for another 24 h to allow spontaneous differentiation of hESCs prior to the immunofluorescence staining experiments.

NIH/3T3 mouse embryonic fibroblasts (ATCC, Manassas, VA, USA) were maintained in a growth medium consisting of high-glucose Dulbecco's modified Eagle's medium (Invitrogen) supplemented with 10% bovine serum (Atlanta Biological, Atlanta, GA, USA), 100 μg mL^{-1} L-glutamine, 100 units mL^{-1} penicillin, and 100 μg mL^{-1} streptomycin. Fresh 0.25% trypsin-EDTA in PBS was used to resuspend NIH/3T3 cells. NIH/3T3 cells were seeded at a low density (3000 cells/cm^2) in the growth medium onto the glass substrates and allowed to spread out overnight before other assays.

For coculture assays single hESCs and NIH/3T3 cells were collected as described above, mixed in hCCM, seeded at a density of 5000 cells/cm^2 for both cell types onto the patterned nanorough glass substrates, and cultured for 48 h prior to fixing and immunostaining.

SEM Specimen Preparation. Cell samples were washed three times with 50 mM Na-cacodylate buffer (pH 7.3; Sigma-Aldrich), fixed for 1 h with 2% glutaraldehyde (Electron Microscopy Sciences, Hatfield, PA, USA) in 50 mM Na-cacodylate buffer, and dehydrated in a graded series of ethanol concentrations through 100% over a period of 1.5 h. Dehydration in 100% ethanol was performed three times. Afterward, dehydrated substrates were dried with liquid CO_2 using a supercritical point dryer (Samdri-PVT-3D, Tousimis, Rockville, MD, USA). Samples were mounted on stubs, sputtered with gold palladium, observed, and photographed under a Hitachi SU8000 ultra-high-resolution SEM machine (Hitachi High Technologies America, Inc., Pleasanton, CA, USA).

Immunofluorescence Staining. In brief, cells were incubated in an ice-cold cytoskeleton buffer (50 mM NaCl, 150 mM sucrose, 3 mM $MgCl_2$, 1 μg mL^{-1} aprotinin, 1 μg mL^{-1} leupeptin, and 1 μg mL^{-1} pepstatin) for 1 min and then permeabilized with 0.5% Triton X-100 (Roche Applied Science, Indianapolis, IN, USA) in the cytoskeleton buffer for 1 min. Detergent-extracted cells were fixed with 4% paraformaldehyde (Electron Microscopy Sciences) in PBS for 30 min and washed three times with PBS. The fixed cells were then incubated with 10% goat serum (Invitrogen) for 1 h and then primary antibodies (produced in either mouse or rabbit) to Oct3/4 (Santa Cruz Biotechnolgy Inc., Santa Cruz, CA, USA), vinculin (Sigma-Aldrich, St. Louis, MO, USA), nonmuscle myosin IIA (Abcam, Cambridge, MA, USA), and E-cadherin (Invitrogen) for 1 h. Alexa Fluor 488 and 555 conjugated goat anti-mouse (or anti-rabbit) IgG secondary antibodies (Invitrogen) were used as secondary antibodies. Alexa Fluor 555 conjugated phalloidin (Invitrogen) and DAPI (Invitrogen) were used for visualization of actin microfilaments and nucleus, respectively.

Western Blot Analysis. Whole cell lysates were prepared from cells, separated on 7.5% SDS-polyacrylamide gel, and transferred to PVDF membranes. The membranes were incubated with 5% milk in PBS for 1 h and then incubated with primary antibodies overnight at 4 °C. Primary antibodies used were as follows: mouse anti-NMMIIA (1:1000; Abcam), mouse anti-E-cadherin (1:1000; Invitrogen), mouse anti-vinculin (1:1000; Sigma-Aldrich), mouse anti-FAK (1:500; BD Biosciences), rabbit anti-Oct4 (1:2000; Santa Cruz), and rabbit anti-β-actin (1:1000; Cell Signaling, Danvers, MA, USA). Blots were incubated with peroxidase-coupled secondary antibodies (Promega, Madison, WI, USA) for 1 h, and protein expression was detected with Super-Signal West Pico chemiluminescent substrate (Thermo Scientific, Rockford, IL, USA).

Quantitative Analysis of Cell Spread Area and Focal Adhesion. Cell spread area and focal adhesion formation were quantified as described previously.[49,50] Briefly, immunofluorescence images of the actin cytoskeleton and vinculin were obtained using a Carl Zeiss Axio Observer Z1 microscope equipped with an AxioCam camera (Carl Zeiss MicroImaging, Thornwood, NY, USA) and a 40× objective (1.3 NA, oil immersion; EC Plan NEOFLUAR). Images were captured using the Axiovision Software (Carl Zeiss MicroImaging) and processed using custom-developed MATLAB programs (Mathworks, Natick, MA, USA). To determine the spread area of each cell, the Canny edge detection method was used to binarize the actin fibers and FAs, and then image dilation, erosion, and fill operations were used to fill in the gaps between the white pixels. The resultant white pixels were summed to quantify cell area. To quantify FA number and area for each cell, the grayscale vinculin image was thresholded to produce a black and white FA image, from which the white pixels, representing FAs, were counted and summed.

Quantification of Cell Population Doubling Time. Cell population doubling time was calculated as the time required for the area of a cell colony to increase 2-fold as previously described.[47,51] The cell colony area was calculated by using the surface area formula for an ellipse ($\pi ab/4$, where a and b are the transverse and conjugate diameters, respectively). Phase-contrast microscopic images of hESC colonies (n = 20) were taken every 24 h after initial cell seeding. ImageJ software (http://rsb.nih.gov/ij) was used to process the images and measure the colony transverse and conjugate diameters. The colony areas were then calculated for different time points (24, 48, 72, and 120 h after cell seeding), and the cell population doubling time was estimated as an exponential function.

Statistics. p-Value was calculated using the Student t-test function in Excel (Microsoft, Seattle, WA, USA).

Conflict of Interest: The authors declare no competing financial interest.

Acknowledgment. We acknowledge financial support from the National Science Foundation (CMMI 1129611 to J.F.), the National Institute of Health (UL1RR024986 to J.F.; R01 DE016530 to P.H.K.; 4R00 CA136759-02 to R.F.), Alzheimer's Association New Investigator Research Grant (R.F.), and the Department of Mechanical Engineering (J.F.) and the NIDCR T32 tissue engineering and regeneration training program (P.H.K.) at the University of Michigan School of Dentistry, Ann Arbor. The Lurie Nanofabrication Facility at the University of Michigan, a member of the National Nanotechnology Infrastructure Network (NNIN) funded by the National Science Foundation, is acknowledged for support in microfabrication.

Supporting Information Available: Additional information and graphics as described in the text. This material is available free of charge *via* the Internet at http://pubs.acs.org.

REFERENCES AND NOTES

1. Geiger, B.; Spatz, J. P.; Bershadsky, A. D. Environmental Sensing through Focal Adhesions. *Nat. Rev. Mol. Cell Biol.* **2009**, *10*, 21–33.
2. Vogel, V.; Sheetz, M. Local Force and Geometry Sensing Regulate Cell Functions. *Nat. Rev. Mol. Cell Biol.* **2006**, *7*, 265–275.
3. Discher, D. E.; Janmey, P.; Wang, Y. L. Tissue Cells Feel and Respond to the Stiffness of Their Substrate. *Science* **2005**, *310*, 1139–1143.
4. Geiger, B.; Bershadsky, A.; Pankov, R.; Yamada, K. M. Transmembrane Extracellular Matrix-Cytoskeleton Crosstalk. *Nat. Rev. Mol. Cell Biol.* **2001**, *2*, 793–805.
5. Li, D.; Zhou, J. X.; Chowdhury, F.; Cheng, J. J.; Wang, N.; Wang, F. Role of Mechanical Factors in Fate Decisions of Stem Cells. *Regen. Med.* **2011**, *6*, 229–240.
6. Kulangara, K.; Leong, K. W. Substrate Topography Shapes Cell Function. *Soft Matter* **2009**, *5*, 4072–4076.
7. Schvartzman, M.; Palma, M.; Sable, J.; Abramson, J.; Hu, X. A.; Sheetz, M. P.; Wind, S. J. Nanolithographic Control of the Spatial Organization of Cellular Adhesion Receptors at the Single-Molecule Level. *Nano Lett.* **2011**, *11*, 1306–1312.
8. Brunetti, V.; Maiorano, G.; Rizzello, L.; Sorce, B.; Sabella, S.; Cingolani, R.; Pompa, P. P. Neurons Sense Nanoscale Roughness with Nanometer Sensitivity. *Proc. Natl. Acad. Sci. U. S. A.* **2010**, *107*, 6264–6269.
9. Stevens, M. M.; George, J. H. Exploring and Engineering the Cell Surface Interface. *Science* **2005**, *310*, 1135–1138.
10. Curtis, A.; Wilkinson, C. Topographical Control of Cells. *Biomaterials* **1997**, *18*, 1573–1583.
11. Yim, E. K.; Reano, R. M.; Pang, S. W.; Yee, A. F.; Chen, C. S.; Leong, K. W. Nanopattern-Induced Changes in Morphology and Motility of Smooth Muscle Cells. *Biomaterials* **2005**, *26*, 5405–5413.
12. Dalby, M. J.; Gadegaard, N.; Tare, R.; Andar, A.; Riehle, M. O.; Herzyk, P.; Wilkinson, C. D. W.; Oreffo, R. O. C. The Control of Human Mesenchymal Cell Differentiation Using Nanoscale Symmetry and Disorder. *Nat. Mater.* **2007**, *6*, 997–1003.
13. Yim, E. K. F.; Pang, S. W.; Leong, K. W. Synthetic Nanostructures Inducing Differentiation of Human Mesenchymal Stem Cells into Neuronal Lineage. *Exp. Cell Res.* **2007**, *313*, 1820–1829.
14. Oh, S.; Brammer, K. S.; Li, Y. S. J.; Teng, D.; Engler, A. J.; Chien, S.; Jin, S. Stem Cell Fate Dictated Solely by Altered Nanotube Dimension. *Proc. Natl. Acad. Sci. U. S. A.* **2009**, *106*, 2130–2135.
15. McMurray, R. J.; Gadegaard, N.; Tsimbouri, P. M.; Burgess, K. V.; McNamara, L. E.; Tare, R.; Murawski, K.; Kingham, E.; Oreffo, R. O. C.; Dalby, M. J. Nanoscale Surfaces for the Long-Term Maintenance of Mesenchymal Stem Cell Phenotype and Multipotency. *Nat. Mater.* **2011**, *10*, 637–644.
16. Yim, E. K. F.; Darling, E. M.; Kulangara, K.; Guilak, F.; Leong, K. W. Nanotopography-Induced Changes in Focal Adhesions, Cytoskeletal Organization, and Mechanical Properties of Human Mesenchymal Stem Cells. *Biomaterials* **2010**, *31*, 1299–1306.
17. Saha, S.; Ji, L.; de Pablo, J. J.; Palecek, S. P. Tgf Beta/Activin/Nodal Pathway in Inhibition of Human Embryonic Stem Cell Differentiation by Mechanical Strain. *Biophys. J.* **2008**, *94*, 4123–4133.
18. Chowdhury, F.; Na, S.; Li, D.; Poh, Y. C.; Tanaka, T. S.; Wang, F.; Wang, N. Material Properties of the Cell Dictate Stress-Induced Spreading and Differentiation in Embryonic Stem Cells. *Nat. Mater.* **2010**, *9*, 82–88.
19. Evans, N. D.; Minelli, C.; Gentleman, E.; LaPointe, V.; Patankar, S. N.; Kallivretaki, M.; Chen, X. Y.; Roberts, C. J.; Stevens, M. M. Substrate Stiffness Affects Early Differentiation Events in Embryonic Stem Cells. *Eur. Cells Mater.* **2009**, *18*, 1–14.
20. Chowdhury, F.; Li, Y.; Poh, Y.-C.; Yokohama-Tamaki, T.; Wang, N.; Tanaka, T. S. Soft Substrates Promote Homogeneous Self-Renewal of Embryonic Stem Cells Via Downregulating Cell-Matrix Tractions. *PLoS One* **2010**, *5*, e15655.
21. Mei, Y.; Saha, K.; Bogatyrev, S. R.; Yang, J.; Hook, A. L.; Kalcioglu, Z. I.; Cho, S. W.; Mitalipova, M.; Pyzocha, N.; Rojas, F.; *et al.* Combinatorial Development of Biomaterials for Clonal Growth of Human Pluripotent Stem Cells. *Nat. Mater.* **2010**, *9*, 768–778.
22. Xie, J. W.; Willerth, S. M.; Li, X. R.; Macewan, M. R.; Rader, A.; Sakiyama-Elbert, S. E.; Xia, Y. N. The Differentiation of Embryonic Stem Cells Seeded on Electrospun Nanofibers into Neural Lineages. *Biomaterials* **2009**, *30*, 354–362.
23. Lee, M. R.; Kwon, K. W.; Jung, H.; Kim, H. N.; Suh, K. Y.; Kim, K.; Kim, K. S. Direct Differentiation of Human Embryonic Stem Cells into Selective Neurons on Nanoscale Ridge/Groove Pattern Arrays. *Biomaterials* **2010**, *31*, 4360–4366.
24. Thomson, J. A.; Itskovitz-Eldor, J.; Shapiro, S. S.; Waknitz, M. A.; Swiergiel, J. J.; Marshall, V. S.; Jones, J. M. Embryonic Stem Cell Lines Derived from Human Blastocysts. *Science* **1998**, *282*, 1145–1147.
25. Jaenisch, R.; Young, R. Stem Cells, the Molecular Circuitry of Pluripotency and Nuclear Reprogramming. *Cell* **2008**, *132*, 567–582.
26. Keller, G. Embryonic Stem Cell Differentiation: Emergence of a New Era in Biology and Medicine. *Genes Dev.* **2005**, *19*, 1129–1155.
27. Saha, K.; Jaenisch, R. Technical Challenges in Using Human Induced Pluripotent Stem Cells to Model Disease. *Cell Stem Cell* **2009**, *5*, 584–595.
28. Colman, A.; Dreesen, O. Pluripotent Stem Cells and Disease Modeling. *Cell Stem Cell* **2009**, *5*, 244–247.
29. Rubin, L. L. Stem Cells and Drug Discovery: The Beginning of a New Era? *Cell* **2008**, *132*, 549–552.
30. Pouton, C. W.; Haynes, J. M. Embryonic Stem Cells as a Source of Models for Drug Discovery. *Nat. Rev. Drug Discovery* **2007**, *6*, 605–616.
31. McNeish, J. Embryonic Stem Cells in Drug Discovery. *Nat. Rev. Drug Discovery* **2004**, *3*, 70–80.
32. Daley, G. Q.; Scadden, D. T. Prospects for Stem Cell-Based Therapy. *Cell* **2008**, *132*, 544–548.
33. Srivastava, D.; Ivey, K. N. Potential of Stem-Cell-Based Therapies for Heart Disease. *Nature* **2006**, *441*, 1097–1099.
34. Lindvall, O.; Kokaia, Z. Stem Cells for the Treatment of Neurological Disorders. *Nature* **2006**, *441*, 1094–1096.
35. Bordignon, C. Stem-Cell Therapies for Blood Diseases. *Nature* **2006**, *441*, 1100–1102.
36. Metwalli, E.; Pantano, C. G. Reactive Ion Etching of Glasses: Composition Dependence. *Nucl. Instrum. Meth. B* **2003**, *207*, 21–27.
37. Leech, P. W. Reactive Ion Etching of Quartz and Silica-Based Glasses in Cf4/Chf3 Plasmas. *Vacuum* **1999**, *55*, 191–196.
38. Choi, D. Y.; Lee, J. H.; Kim, D. S.; Jung, S. T. Formation of Plasma Induced Surface Damage in Silica Glass Etching for Optical Waveguides. *J. Appl. Phys.* **2004**, *95*, 8400–8407.
39. Braam, S. R.; Zeinstra, L.; Litjens, S.; Ward-van Oostwaard, D.; van den Brink, S.; van Laake, L.; Lebrin, F.; Kats, P.; Hochstenbach, R.; Passier, R.; *et al.* Recombinant Vitronectin Is a Functionally Defined Substrate That Supports Human Embryonic Stem Cell Self-Renewal Via Avβ5 Integrin. *Stem Cells* **2008**, *26*, 2257–2265.
40. McBeath, R.; Pirone, D. M.; Nelson, C. M.; Bhadriraju, K.; Chen, C. S. Cell Shape, Cytoskeletal Tension, and Rhoa Regulate Stem Cell Lineage Commitment. *Dev. Cell* **2004**, *6*, 483–495.
41. Engler, A. J.; Sen, S.; Sweeney, H. L.; Discher, D. E. Matrix Elasticity Directs Stem Cell Lineage Specification. *Cell* **2006**, *126*, 677–689.
42. Li, D.; Zhou, J. X.; Wang, L.; Shin, M. E.; Su, P.; Lei, X. H.; Kuang, H. B.; Guo, W. X.; Yang, H.; Cheng, L. Z.; *et al.* Integrated Biochemical and Mechanical Signals Regulate Multifaceted Human Embryonic Stem Cell Functions. *J. Cell. Biol.* **2010**, *191*, 631–644.
43. Chen, G.; Hou, Z.; Gulbranson, D. R.; Thomson, J. A. Actin-Myosin Contractility Is Responsible for the Reduced

Viability of Dissociated Human Embryonic Stem Cells. *Cell Stem Cell* **2010**, *7*, 240–248.
44. Ohgushi, M.; Matsumura, M.; Eiraku, M.; Murakami, K.; Aramaki, T.; Nishiyama, A.; Muguruma, K.; Nakano, T.; Suga, H.; Ueno, M.; *et al*. Molecular Pathway and Cell State Responsible for Dissociation-Induced Apoptosis in Human Pluripotent Stem Cells. *Cell Stem Cell* **2010**, *7*, 225–239.
45. Walker, A.; Su, H.; Conti, M. A.; Harb, N.; Adelstein, R. S.; Sato, N. Non-Muscle Myosin II Regulates Survival Threshold of Pluripotent Stem Cells. *Nat. Commun.* **2010**, *1*, 71.
46. Peerani, R.; Rao, B. M.; Bauwens, C.; Yin, T.; Wood, G. A.; Nagy, A.; Kumacheva, E.; Zandstra, P. W. Niche-Mediated Control of Human Embryonic Stem Cell Self-Renewal and Differentiation. *Embo J.* **2007**, *26*, 4744–4755.
47. Villa-Diaz, L. G.; Nandivada, H.; Ding, J.; Nogueira-De-Souza, N. C.; Krebsbach, P. H.; O'Shea, K. S.; Lahann, J.; Smith, G. D. Synthetic Polymer Coatings for Long-Term Growth of Human Embryonic Stem Cells. *Nat. Biotechnol.* **2010**, *28*, 581–583.
48. Nandivada, H.; Villa-Diaz, L. G.; O'Shea, K. S.; Smith, G. D.; Krebsbach, P. H.; Lahann, J. Fabrication of Synthetic Polymer Coatings and Their Use in Feeder-Free Culture of Human Embryonic Stem Cells. *Nat. Protoc.* **2011**, *6*, 1037–1043.
49. Fu, J. P.; Wang, Y. K.; Yang, M. T.; Desai, R. A.; Yu, X. A.; Liu, Z. J.; Chen, C. S. Mechanical Regulation of Cell Function with Geometrically Modulated Elastomeric Substrates. *Nat. Methods* **2010**, *7*, 733–795.
50. Yang, M. T.; Sniadecki, N. J.; Chen, C. S. Geometric Considerations of Micro- to Nanoscale Elastomeric Post Arrays to Study Cellular Traction Forces. *Adv. Mater.* **2007**, *19*, 3119–3123.
51. Reubinoff, B. E.; Pera, M. F.; Vajta, G.; Trounson, A. O. Effective Cryopreservation of Human Embryonic Stem Cells by the Open Pulled Straw Vitrification Method. *Hum. Reprod.* **2001**, *16*, 2187–2194.